Materials Today Communications 35 (2023) 106289

Contents lists available at ScienceDirect

Materials Today Communications

journal homepage: www.elsevier.com/locate/mtcomm

Topological phonons and low lattice thermal conductivity of Li_2CaX (X = Sn and Pb) type Heusler compounds

Vineet Kumar Sharma [a], V. Kanchana [a,*], Mayanak K. Gupta [b,c], Ranjan Mittal [b,c]

[a] Department of Physics, Indian Institute of Technology Hyderabad, Kandi 502285, Sangareddy, Telangana, India
[b] Solid state physics division, Bhabha Atomic Research Centre Trombay, Mumbai 400085, India
[c] Homi Bhabha National Institute, Anushaktinagar, Mumbai 400094, India

ARTICLE INFO

Keywords:
Topological phonons
Lattice thermal conductivity
Thermoelectric figure of merit

ABSTRACT

The topological phonons, electronic structure, and transport properties of Li_2CaX (X = Sn and Pb) have been investigated using first-principles. Topological phononic states are facilitated by Dirac-like band crossings observed in optical phonon branches, which are ensured by calculated surface states in the (001) plane. Li_2CaPb has very low lattice thermal conductivity(κ_l), as evidenced by shorter phonon lifetime, acoustic phonon mode dispersion, and low Debye temperature. The value of κ_l is low at high temperatures due to Dirac-like crossings in optical phonon branches exhibiting non-trivial topological properties. The inclusion of hybrid functional transits Li_2CaPb into an indirect bandgap semiconductor. Li_2CaPb has a figure of merit of 0.15 for holes and 0.2 for electrons at 500 K. Topological phonons combined with promising transport features in Li_2CaX (X = Sn and Pb) may be desirable for future device applications.

1. Introduction

The unprecedented technological advancement and modern civilization require huge amounts of energy primarily derived from non-renewable sources like coal and petroleum. The limited quantity of these energy sources led to the emergence of technologies like solar cells, photovoltaic cells, biofuels, etc. Thermoelectricity is one among these emerging technologies, which utilizes the waste heat lost in the environment as an input, and converts it into useful electricity and vice-versa. This technology might significantly reduce energy consumption and save huge economic losses [1]. Although waste-heat recovery can minimize the energy crisis, current TE devices are too expensive and inefficient to support widespread use [2,3]. Traditional thermoelectric materials such as Bi_2Te_3, PbTe, and $Si_{1-x}Ge_x$ are well-known for their high performance at intermediate temperatures [4]. A surplus amount of research has been undertaken over the past few years to identify highly efficient thermoelectric materials [4–12]. A dimensionless quantity that characterizes any thermoelectric material's efficiency is called the figure of Merit (ZT). To achieve a high figure of merit, one should look for a material with high thermopower(S), high electrical conductivity (σ), and low thermal conductivity ($\kappa = \kappa_e + \kappa_l$ 'sum of electronic and lattice contributions'), which can be understood from the relation, "$ZT = S^2\ \sigma T/\kappa$". The interdependency of thermopower, electrical conductivity, and electronic thermal conductivity (κ_e) poses a significant challenge for researchers to achieve higher efficiency. Certain techniques, such as nanostructuring [5,6] and choosing materials that are more susceptible to scattering (Clathrates, etc.) [13] may result in low lattice thermal conductivity and enable ZT values higher than 1. This prompted further research in the field of thermoelectricity, which resulted in the realization of new classes of effective TE materials such as clathrates [14], skutterudites [15], group IV-VI compounds [16], Zintl phase [17]. One of the recent studies revealed that the topological phonons in triple point metals suppress the lattice thermal conductivity and enhance TE performance [18]. Previous studies on the Heusler compounds [19–23] have reported their promising electrical, magnetic, and transport properties, but these are unsuitable for real TE applications due to high lattice thermal conductivity. A few Lanthanum-based half-Heuslers [24] and the alkali-based full-Heuslers [25] were projected to have very low κ_l at 300 K using machine learning methods and high-throughput computations, respectively. Bhattacharya et al. reported the high power factor for a few Ni-based half-Heusler alloys [26]. Heusler compounds containing lighter elements like Li are suitable for their potential storage applications [27]. The previous findings on various Heusler compounds inspire us to investigate Li-based full-Heusler compounds such as Li_2CaSn and Li_2CaPb. Besides experimental synthesis by Stoiber et al. [28], one earlier study [29] provides a first-principles analysis of structural, electrical, and thermal properties. There are no studies describing the thermoelectric properties of these materials, paving the way for

* Corresponding author.
E-mail address: kanchana@iith.ac.in (V. Kanchana).

https://doi.org/10.1016/j.mtcomm.2023.106289
Received 11 March 2023; Received in revised form 15 May 2023; Accepted 22 May 2023
Available online 27 May 2023

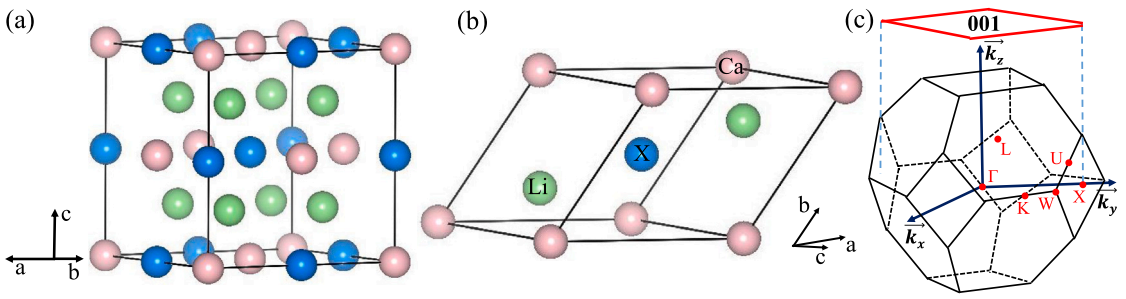

Fig. 1. (a) The conventional unit cell with four formula units, (b) The primitive unit cell. Ca, X(Sn and Pb), and Li atoms are represented by light pink, blue, and green spheres, respectively. (c) The irreducible Brillouin zone for face-centered cubic symmetry. Red dots displays high symmetry points. (001) plane is shown by the top surface. (For interpretation of the references to color in this figure legend, the reader is referred to the web version of this article.)

Table 1
Computed lattice parameters of Li_2CaX and associated experimental parameters [28].

Compound	Experiment [28] a (Å)	GGA-PBE [32] a (Å)	LDA [33] a (Å)
Li_2CaSn	6.94	6.96	6.75
Li_2CaPb	6.98	7.07	6.83

Table 2
Elastic constants and other mechanical properties of Li_2CaX.

Elastic properties	Li_2CaSn	Li_2CaPb
C_{11} (GPa)	59.47	48.84
C_{12} (GPa)	21.24	18.80
C_{44} (GPa)	34.48	28.22
B (GPa)	33.98	28.81
G (GPa)	27.21	21.91
E (GPa)	64.43	52.43
B/G	1.24	1.37
σ	0.18	0.19
θ_D	336.32	247.54
Melting point(T_m)	900 K ± 300 K	840 K ± 300 K

further research into these materials. The present work highlights the thermal properties, topological phonons, and electronic and thermoelectric properties of these full-Heusler compounds. The organization of this paper is as follows: the methods used to compute different properties are presented in Section 2, followed by a description of the mechanical properties, phonon band spectrum, and their topological features in Section 3. Section 4 describes the lattice thermal transport. The electronic structural properties with GGA-PBE and HSE (Heyd–Scuseria–Ernzerhof) functionals are discussed subsequently, followed by thermoelectric properties, and a summary is given in the last section.

2. Methodology and crystal structure

The structural optimization is performed using VASP [30,31] for different exchange–correlation functionals, GGA-PBE [32] and LDA [33], and found that GGA parameters are consistent with experiments [28] [Table 1]. Monkhorst-pack scheme [34] with K-mesh of 16 × 16 × 16 is used for Brillouin zone sampling. The energy convergence of 10^{-8} eV and force tolerance factor of 10^{-2} eV/Åare chosen to calculate well-converged energy eigenvalues. The plane-wave energy cut-off is set to 900 eV. Tetrahedron method [35] is used to integrate the irreducible Brillouin zone. The force constants are computed using VASP to plot the phonon dispersion using phonopy [36]. The tight-binding Hamiltonian [37,38] was generated for phonons to compute the topological properties like surface states and bulk gap plane using the Wannier-Tools package [39,40]. Thermal properties like lattice thermal conductivity are calculated via the supercell approach with a displacement of 0.03 Å using the phono3py package [41]. Both the GGA-PBE [32] and HSE (Heyd–Scuseria–Ernzerhof) [42] functionals are used to analyze the electronic structure properties. The semi-classical Boltzmann transport theory implemented in the Boltztrap code [43] is used to compute thermoelectric coefficients within two approximations: relaxation time approximation(RTA) and rigid band approximation(RBA). Fig. 1(a & b) display the crystal structure of Li_2CaX (where, X = Sn and Pb). The irreducible Brillouin zone illustrating high symmetry points is given in Fig. 1(c) .

3. Results and discussion

3.1. Mechanical and dynamical properties

Examining the mechanical and dynamical stabilities is the primary step to validate any system's structural stability. The mechanical stability of these compounds is ensured by the computed elastic constants, which meet Born's mechanical stability criterion for cubic symmetry [44]. The elastic constants and other mechanical parameters are listed in Table 2. The calculated bulk moduli agree well with earlier reported values determined using energy-volume fitting curves [29]. There are no experimental reports available so far. B/G ratio and Poisson ratio values are lesser than their critical values (1.75 and 0.26, respectively), which indicate the brittle nature of these compounds [45]. A negative value of Cauchy pressure (C_{12} - C_{44}) also supports brittle nature here. The Debye temperature (θ_D) is calculated using the empirical relations in terms of sound velocities [46], which plays a vital role in defining any material's high and low operating temperature ranges. It is also linked with other thermal properties like specific heat, which impacts lattice thermal conductivity. The computed value of θ_D is low, indicating the low lattice thermal conductivity in the examined compounds.

The phonon dispersion is plotted to test the dynamical stability, as illustrated in Fig. 2. All phonon branches are positive, demonstrating the dynamical stability of Li_2CaX (where, X = Sn and Pb). The difference in atomic weight of constituent elements causes a frequency gap between high- and low-frequency optical modes. A detailed examination of Li_2CaPb phonon dispersion reveals a minor gap between acoustic and low-frequency optical modes. The acoustic phonon modes of Li_2CaPb are less dispersive than those of Li_2CaSn, implying that Li_2CaPb has a lower group velocity.

Dirac-like dispersion observed in the optical phonon branches at and around the high symmetry point 'W', motivates us to investigate the topological properties of these phononic states. Li_2CaPb has been taken as an example to highlight the topological features in these Heusler compounds. To begin with, the tight-binding Hamiltonian has been generated using the Wannier90 package to visualize the surface states and iso-frequency spectrum in the (001) plane. Fig. 3 depicts the computed topological properties of Li_2CaPb. We project the topological character of both low- and high-frequency optical phonon modes. Fig. 3(b) displays the surface state plot for optical phonons in frequency ranging from 3–4 THz. We observe the drumhead surface states emanating from bulk phonon crossings. In general, a drumhead surface state is always connected with a nodal line, and the same[NL1] is

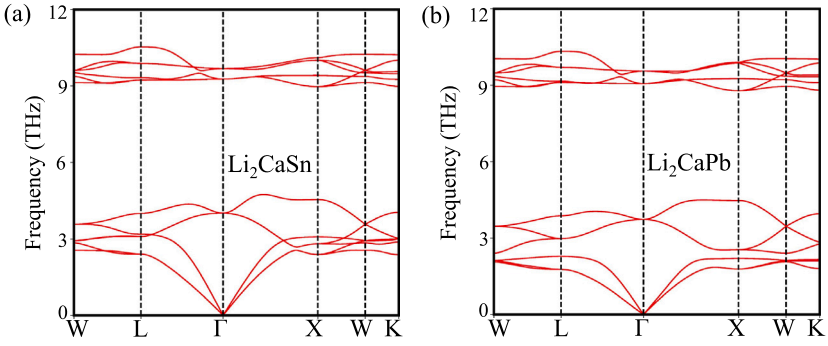

Fig. 2. The phonon spectrum plotted along high symmetry points, as mentioned in IBZ Fig. 1(a) for Li_2CaSn in (a) and for Li_2CaPb in (b).

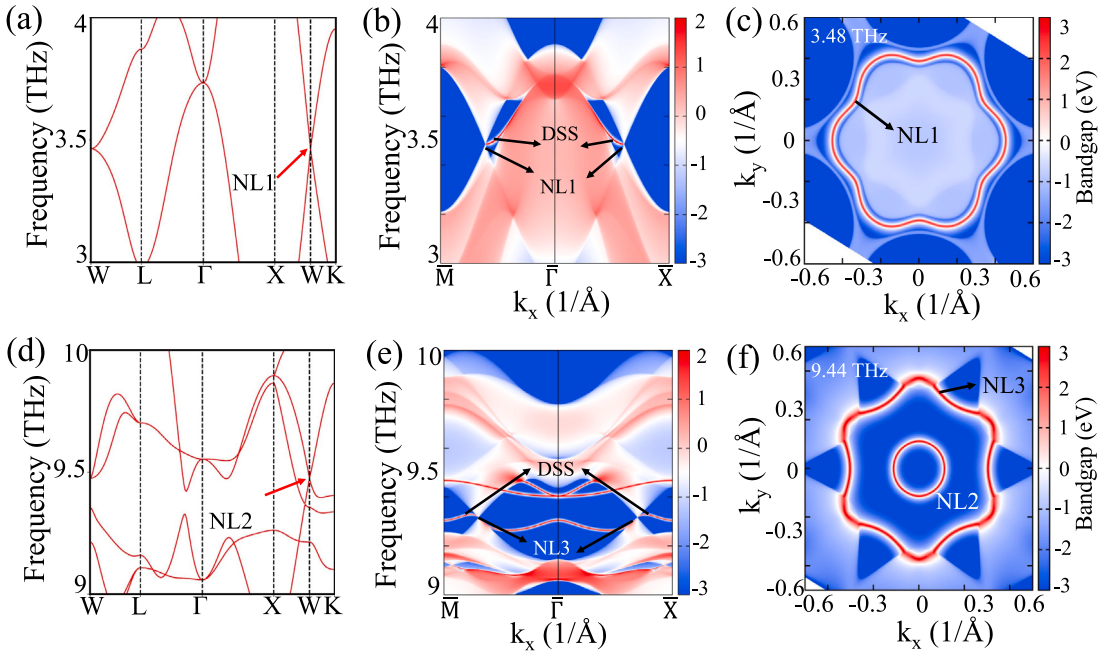

Fig. 3. (a) Li_2CaPb phonon spectrum in a frequency range between 3–4 THz. The red arrow indicates the nodal line. (b) Surface state spectrum plotted in (001) plane. Black arrows mark drumhead surface states and nodal lines. (c) Constant frequency contour plot at 3.48 THz displays the nodal line. (d) Li_2CaPb phonon spectrum in a frequency range between 9–10 THz. (e) Surface state spectrum in (001) plane for optical modes shown in Fig.(d). (e) Constant frequency contour plot at 9.44 THz displays the nodal lines. (For interpretation of the references to color in this figure legend, the reader is referred to the web version of this article.)

depicted in an iso-frequency plot at 3.48 THz [Fig. 3(c)]. Figs. 3(d, e, & f) depict the topological features of high-frequency optical phonon branches [frequency range 9–10 THz]. These optical branches have multi-Dirac-like crossings around high-symmetry point 'W'. The surface states for these modes are given in Fig. 3(e), displaying the surface states arising from the bulk band crossings similar to the low-frequency case. Nodal lines[NL2 & NL3] corresponding to these crossings are given in Fig. 3(f). The symmetry analysis should be considered while addressing the topological properties of any system, and the same is included here. The investigated system is non-magnetic and hosts both inversion and time-reversal symmetries. Nine mirror planes including M_x, M_y, M_z, M_{xy}, $M_{x\bar{y}}$, M_{yz}, $M_{y\bar{z}}$, M_{xz} and $M_{x\bar{z}}$ are present in this face-centered cubic system. The nodal lines observed in the bulk bandgap calculations are found in the (001) plane and are protected by mirror symmetries M_x, M_y, M_{xy} and $M_{x\bar{y}}$. To check the topological character of these nodal lines, we have calculated the Berry phase using the relation given in literature [47]. The calculated value of the Berry phase for the k-loop enclosing NL1 is π, and it is zero for the remaining two nodal lines denoted as NL2 and NL3. It infers the non-trivial topology in phononic states forming the NL1, whereas the phononic states in the high-frequency region are topologically trivial.

3.2. Lattice thermal transport

The lattice thermal conductivity (κ_l) is estimated to observe the influence of topological phonons on thermal transport. Fig. 4(a) shows the temperature-dependent κ_l plotted between 100 K to 500 K. It decreases as the temperature rises, which is a usual trend. The plots reveal a significant difference in κ_l values of both compounds. Li_2CaPb has an extremely low κ_l, which may entice potential applications in thermoelectricity. The phonon-lifetime as a function of phonon-frequency at 300 K is also calculated to examine the room temperature effect on κ_l [Fig. 4(b & c)]. The black dots represent phonon modes, while the color bar shows their density. Li_2CaPb has a much lower phonon-lifetime than Li_2CaSn. The lower κ_l for Li_2CaPb is due to acoustic phonon mode dispersion and shorter phonon-lifetime. Fig. 4(d) depicts the accumulative lattice thermal conductivity as a function of the mean free path. Li_2CaPb(200 Å) has a much lower saturated value of mean free path than Li_2CaSn (1000 Å). This saturation value is crucial in determining whether any material is appropriate for nanostructure engineering. The saturation value of the mean free path is greater than the grain size of the materials studied, implying that future nanostructure engineering will be possible. It may further reduce κ_l and increase TE performance. To check the contribution of optical phonon modes to κ_l,

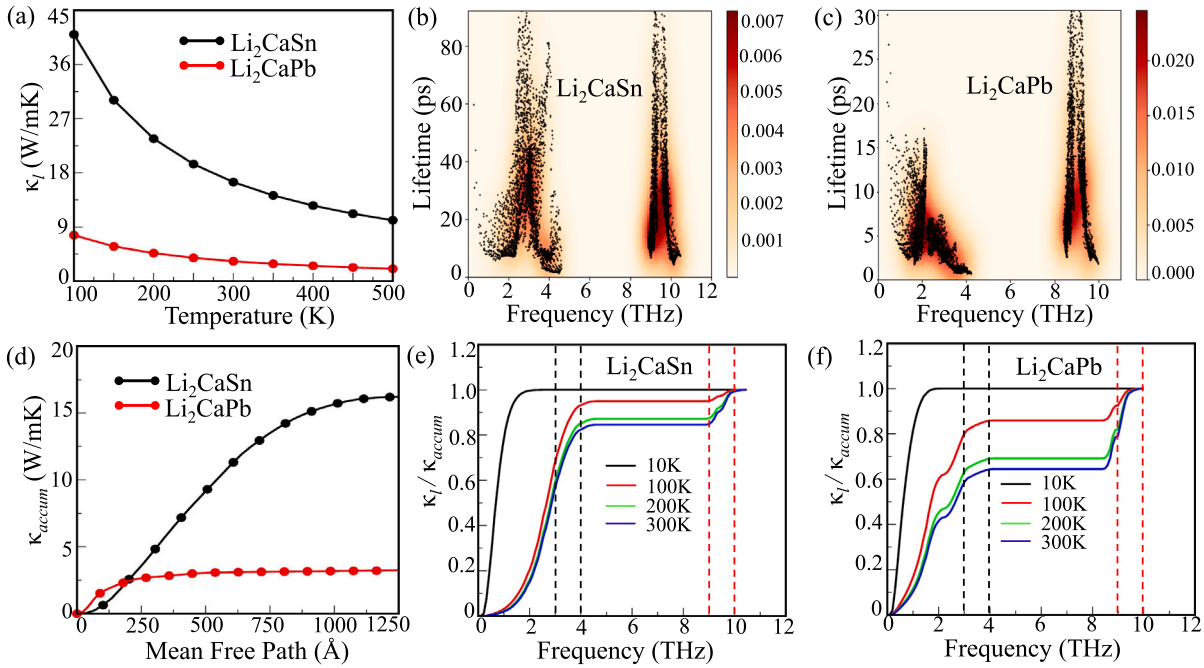

Fig. 4. The temperature-dependent lattice thermal conductivity in (a), (b–c) the phonon-lifetime for Li_2CaSn and Li_2CaPb respectively, at 300 K, the color bar represents the density of phonon modes. (d) accumulative lattice thermal conductivity as a function of the mean free path at 300 K. (e, f) Frequency-dependent κ_l / κ_{accum} for various temperature values.

the ratio of κ_l and κ_{accum} is plotted at different temperatures [Fig. 4(e & f)]. κ_l is entirely dominated by acoustic modes in a low-temperature regime, as seen from the plots for 10 K. The optical mode contribution to κ_l increases as the temperature rises. This analysis suggests that the optical branches enable low κ_l in these explored compounds. The topological features observed in optical phonon modes responsible for flattened surface states may cause more scattering, leading to a low κ_l. These Heusler compounds may offer good TE performance due to their low κ_l.

3.3. Electronic structure properties

The electronic band structure of these full-Heusler compounds is computed using equilibrium lattice constants along the high symmetry directions in the irreducible Brillouin zone [Fig. 1(c)]. Fig. 5(a) depicts the electronic band structure for Li_2CaSn using the GGA-PBE functional [32]. The existence of hole and electron-type bands in the energy eigenstates at the Fermi level verifies the system's semimetallic nature. Fig. 5(b) depicts the projected band structure to understand partial orbital contributions to these states. Ca - *s, d* and X - *p* orbitals contribute most to the bands near the Fermi level. The lack of experimental reports on electronic structure properties motivates us to incorporate HSE (Heyd–Scuseria–Ernzerhof) [42] functional here, which has drastically changed the band structure profile, especially in the case of Li_2CaPb which turns out to be an indirect bandgap semiconductor with a bandgap of 0.03 eV [Fig. 6(c)] from a semimetal [Fig. 6(a)]. Fig. 6(b) shows the orbital decomposed band structure of Li_2CaPb. The noticeable changes in electronic structural properties with HSE functional and low lattice thermal conductivity indicate that these compounds might be appealing for potential thermoelectric properties described in the next section.

4. Thermoelectric properties

The thermoelectric properties for these full-Heusler compounds are computed as a function of temperature for fixed carrier concentration 10^{19} cm^{-3} using HSE (Heyd–Scuseria–Ernzerhof) [42] functional.

Table 3
Comparative studies of calculated thermoelectric figure of merit with values reported for other full-Heusler compounds at 500 K.

Compounds	ZT
Fe_2ScP [48]	0.16
Fe_2ScAs [48]	~ 0.2
Ru_2VSn [49]	~ 0.05
Co_2CrX(X = Al, Si, Ge & Sn)[50]	~ (10^{-4} – 10^{-3})
Ru_2NbAl [51]	~ 10^{-2}
Li_2CaPb (current work)	0.2

Fig. 7(a & b) display the thermopower for holes and electrons. The magnitude of thermopower increases with temperature. Thermopower is plotted up to 500 K since the examined systems are brittle and have low melting temperatures. The thermopower of Li_2CaSn is higher than that for Li_2CaPb. The magnitudes of thermopower for electrons are nearly the same for both compounds for temperatures ranging between 400 K to 500 K. The bipolar conduction affects the magnitude of thermopower, notably in Li_2CaSn. The magnitude of thermopower is around 100 μV/K and 175 μV/K for holes and electrons, respectively, at 500 K. The increasing trend in thermopower with temperature is a good sign for high TE performance. Following that, the electrical conductivity scaled by relaxation time (σ/τ) is calculated [Figs. 7(c & d)]. σ/τ is higher for Li_2CaPb for both the carriers. The holes show a decremental effect with temperature, whereas electrons show a mixed trend with a decremental effect till 300 K and start increasing beyond this value. σ/τ is higher for holes than for electrons. The combined effect of thermopower and σ/τ can be observed from the power factor scaled by relaxation time ($S^2\sigma/\tau$) calculations. The calculated $S^2\sigma/\tau$ is displayed in Figs. 7(e & f). Thermopower significantly impacts the $S^2\sigma/\tau$ plots of holes and electrons. The effect of nearly the same thermopower values for electrons is reflected in $S^2\sigma/\tau$ values of these carriers. The lack of experimental data available for the electrical conductivity or resistivity of these compounds motivated to assume the relaxation time to be 10^{-14} s to determine the absolute value of the electronic part of thermal conductivity (κ_e) and figure of merit

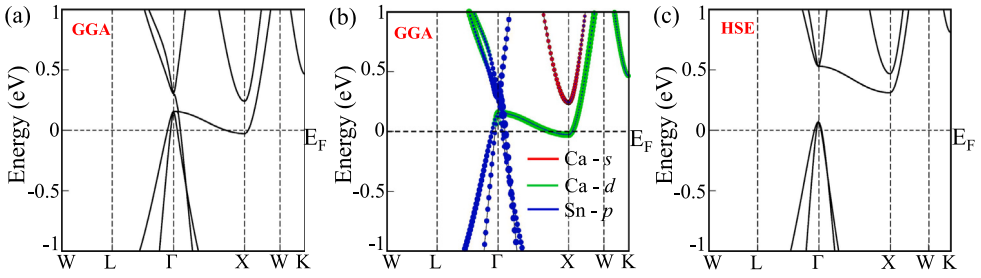

Fig. 5. (a) Li_2CaSn electronic band structure, (b) orbital projected band structure using GGA functional, (c) the electronic band structure using HSE (Heyd–Scuseria–Ernzerhof) [42] functional.

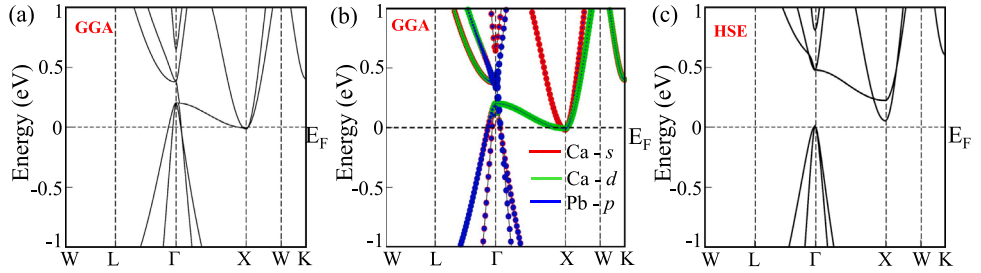

Fig. 6. (a) Li_2CaPb electronic band structure, (b) orbital projected band structure using GGA functional, (c) the electronic band structure using HSE (Heyd–Scuseria–Ernzerhof) [42] functional.

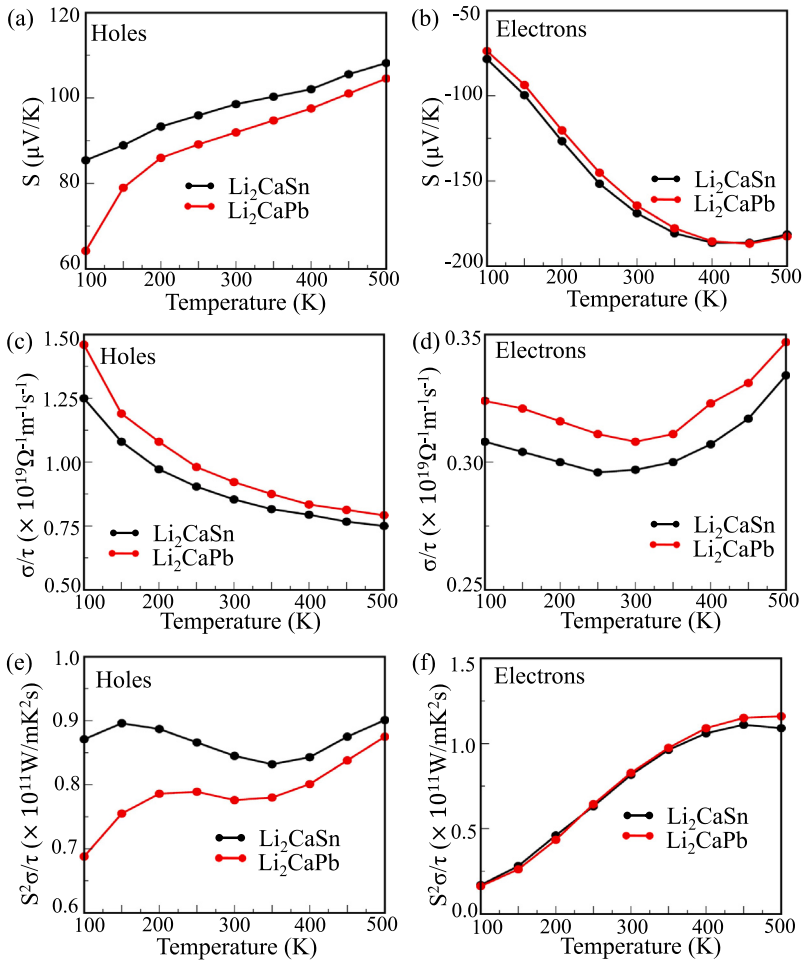

Fig. 7. (a–b) Temperature-dependent thermopower for holes and electrons respectively, (c–d) Variation in the electrical conductivity scaled by relaxation time with temperature for holes and electrons respectively. (e–f) Temperature-dependent power factor scaled by relaxation time for holes and electrons respectively.

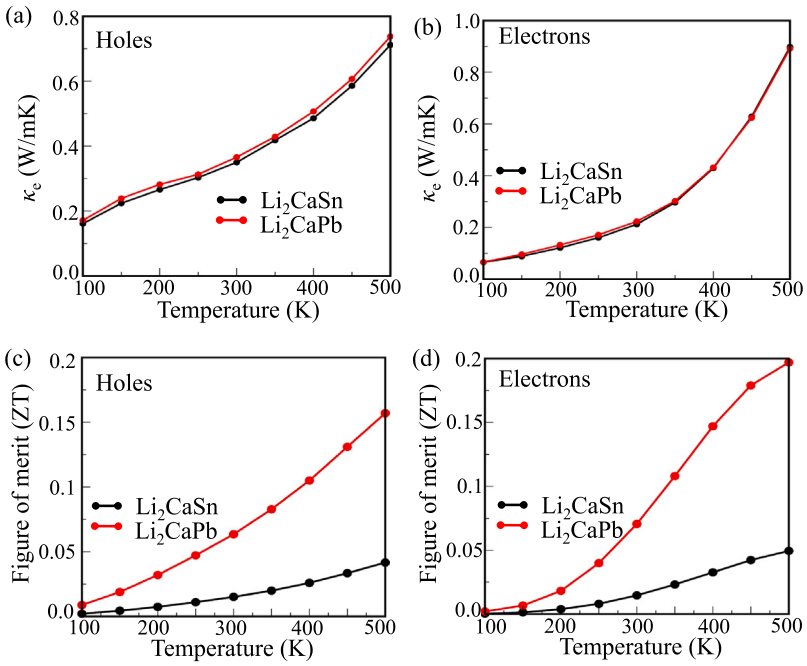

Fig. 8. (a–b) Absolute electronic part of thermal conductivity as a function of temperature for holes and electrons respectively, (c–d) Variation in the figure of merit with temperature for holes and electrons respectively. The estimated relaxation time value is 10^{-14} s.

(ZT). This relaxation time value aligns with previous studies on Heusler compounds [51–54]. The calculated κ_e and ZT are shown in Fig. 8. κ_e increases with temperature for both carriers, which is an usual trend [Figs. 8(a & b)]. As the $S^2\sigma/\tau$ values for both compounds do not differ significantly, the effect of κ_l becomes essential to determine the figure of merit. The figure of merit for both the compounds increases with temperature [Figs. 8(c & d)]. The figure of merit values for Li_2CaSn are nearly 0.05 for both carriers at 500 K. Li_2CaPb stands out differently with an appreciable figure of merit values of 0.15 for holes and 0.20 for electrons, respectively, at 500 K. The comparative analysis with a few other full-Heusler compounds is given in Table 3, which reckons that these investigated compounds have displayed promising TE properties and may open avenues for experimentalists for further exploration.

5. Conclusion

In summary, this article elucidates the electronic structure and thermoelectric properties of full-Heusler compounds Li_2CaX (where, X = Sn and Pb) using density functional theory. The calculated elastic constants are positive and meet Born's mechanical stability criteria, ensuring mechanical stability. No negative phonon mode is seen in the phonon spectrum, which guarantees the dynamical stability of these compounds. Highly linearized optical phonon modes signal the topological features in these Heusler compounds, and the same is manifested by the drumhead surface states emanating from bulk phonon crossings and nodal lines shown in iso-frequency plots calculated in the (001) plane. The π Berry phase for the nodal line corresponding to mid-frequency phononic surface states ensure non-trivial nature, whereas the high-frequency phononic surface states are topologically trivial with zero Berry phase. The lattice thermal conductivity calculations reveal the very low κ_l for Li_2CaPb as the phonon-lifetime is very short for the same. The investigated compounds are semimetallic, as observed from the calculated electronic band structures. The inclusion of HSE functional turned Li_2CaPb into an indirect bandgap semiconductor with a tiny bandgap of 0.03 eV. These noticeable changes and low lattice thermal conductivity prompt an idea to compute the thermoelectric properties here. The thermopower values for both compounds are almost the same, but the lower κ_l of Li_2CaPb makes it a more efficient TE material. The calculated thermoelectric figure of merit values is nearly 0.05 in Li_2CaSn for both the carriers and Li_2CaPb has ZT values of 0.15 and 0.2 at 500 K for holes and electrons. The examined compounds have shown promising TE properties that await future experimental verification.

CRediT authorship contribution statement

Vineet Kumar Sharma: Executing the problem, Running the calculations, Data analysis, Manuscript preparation. **V. Kanchana:** Problem identification, Data analysis, Discussion of results, Manuscript preparation and editing. **Mayanak K. Gupta:** Analysis of results, Editing the manuscript, Discussions. **Ranjan Mittal:** Running a part of the program, Discussion of results, Analysis, Manuscript editing.

Declaration of competing interest

The authors declare that they have no known competing financial interests or personal relationships that could have appeared to influence the work reported in this paper.

Data availability

Data will be made available on request.

Acknowledgments

V.K.S. and V.K. express their gratitude to I.I.T. Hyderabad for providing computational resources. The authors acknowledge financial support from the BRNS project with sanction No. 58/14/13/2019-BRNS. V.K.S. thanks the Ministry of Education, India for the research fellowship. V.K. would like to thank DST-FIST (SR/FST/PSI-215/2016) for the financial support.

References

[1] J.B. Neaton, Thermoelectricity at the gate, Nature Nanotechnol. 9 (11) (2014) 876–877.

[2] S. LeBlanc, S.K. Yee, M.L. Scullin, C. Dames, K.E. Goodson, Material and manufacturing cost considerations for thermoelectrics, Renew. Sustain. Energy Rev. 32 (2014) 313–327.

[3] M.W. Gaultois, T.D. Sparks, C.K. Borg, R. Seshadri, W.D. Bonificio, D.R. Clarke, Data-driven review of thermoelectric materials: performance and resource considerations, Chem. Mater. 25 (15) (2013) 2911–2920.

[4] G.J. Snyder, E.S. Toberer, Complex thermoelectric materials, in: Materials for Sustainable Energy: A Collection of Peer-Reviewed Research and Review Articles from Nature Publishing Group, World Scientific, 2011, pp. 101–110.

[5] D. Medlin, G. Snyder, Interfaces in bulk thermoelectric materials: a review for current opinion in colloid and interface science, Curr. Opin. Colloid Interface Sci. 14 (4) (2009) 226–235.

[6] A. Minnich, M.S. Dresselhaus, Z. Ren, G. Chen, Bulk nanostructured thermoelectric materials: current research and future prospects, Energy Environ. Sci. 2 (5) (2009) 466–479.

[7] A. Shakouri, Recent developments in semiconductor thermoelectric physics and materials, Annu. Rev. Mater. Res. 41 (2011) 399–431.

[8] T.M. Tritt, Thermoelectric phenomena, materials, and applications, Annu. Rev. Mater. Res. 41 (2011) 433–448.

[9] M. Zebarjadi, K. Esfarjani, M. Dresselhaus, Z. Ren, G. Chen, Perspectives on thermoelectrics: from fundamentals to device applications, Energy Environ. Sci. 5 (1) (2012) 5147–5162.

[10] C.J. Vineis, A. Shakouri, A. Majumdar, M.G. Kanatzidis, Nanostructured thermoelectrics: big efficiency gains from small features, Adv. Mater. 22 (36) (2010) 3970–3980.

[11] J.C. Sootsman, DY and kanatzidis, MG angew, Chem. Int. Ed 48 (2009) 8616–8639.

[12] M.S. Dresselhaus, G. Chen, M.Y. Tang, R. Yang, H. Lee, D. Wang, Z. Ren, J.-P. Fleurial, P. Gogna, New directions for low-dimensional thermoelectric materials, Adv. Mater. 19 (8) (2007) 1043–1053.

[13] G. Nolas, J. Cohn, G. Slack, S. Schujman, Semiconducting ge clathrates: Promising candidates for thermoelectric applications, Appl. Phys. Lett. 73 (2) (1998) 178–180.

[14] T. Takabatake, K. Suekuni, T. Nakayama, E. Kaneshita, Publisher's note: Phonon-glass electron-crystal thermoelectric clathrates: Experiments and theory [rev. Mod. Phys. 86, 669 (2014)], Rev. Modern Phys. 86 (2) (2014) 841.

[15] X. Meng, Z. Liu, B. Cui, D. Qin, H. Geng, W. Cai, L. Fu, J. He, Z. Ren, J. Sui, Grain boundary engineering for achieving high thermoelectric performance in n-type skutterudites, Adv. Energy Mater. 7 (13) (2017) 1602582.

[16] W. He, D. Wang, H. Wu, Y. Xiao, Y. Zhang, D. He, Y. Feng, Y.-J. Hao, J.-F. Dong, R. Chetty, et al., High thermoelectric performance in low-cost SnS0. 91Se0. 09 crystals, Science 365 (6460) (2019) 1418–1424.

[17] S. Huang, H. Liu, D. Fan, P. Jiang, J. Liang, G. Cao, R. Liang, J. Shi, First-principles study of the thermoelectric properties of the Zintl compound KSnSb, J. Phys. Chem. C 122 (8) (2018) 4217–4223.

[18] S. Singh, Q. Wu, C. Yue, A.H. Romero, A.A. Soluyanov, Topological phonons and thermoelectricity in triple-point metals, Phys. Rev. Mater. 2 (11) (2018) 114204.

[19] C. Fu, S. Bai, Y. Liu, Y. Tang, L. Chen, X. Zhao, T. Zhu, Realizing high figure of merit in heavy-band p-type half-Heusler thermoelectric materials, Nature Commun. 6 (1) (2015) 1–7.

[20] R. He, D. Kraemer, J. Mao, L. Zeng, Q. Jie, Y. Lan, C. Li, J. Shuai, H.S. Kim, Y. Liu, et al., Achieving high power factor and output power density in p-type half-Heuslers Nb1-xTixFeSb, Proc. Natl. Acad. Sci. 113 (48) (2016) 13576–13581.

[21] P.D. Patel, S. Shinde, S.D. Gupta, P.K. Jha, Investigation of structural and elastic stability, electronic, magnetic, thermoelectric, lattice-dynamical and thermodynamical properties of spin gapless semiconducting Heusler alloy Zr2MnIn using DFT approach, J. Electron. Mater. 48 (3) (2019) 1634–1642.

[22] P.D. Patel, S.M. Shinde, S.D. Gupta, P.K. Jha, A promising thermoelectric response of fully compensated ferrimagnetic spin gapless semiconducting Heusler alloy Zr2MnAl at high temperature: Dft study, Mater. Res. Express 6 (7) (2019) 076307.

[23] P.D. Patel, J.B. Pandya, S.M. Shinde, S.D. Gupta, S. Narayan, P.K. Jha, Investigation of full-heusler compound Mn2MgGe for magnetism, spintronics and thermoelectric applications: DFT study, Comput. Condens. Matter 23 (2020) e00472.

[24] J. Carrete, W. Li, N. Mingo, S. Wang, S. Curtarolo, Finding unprecedentedly low-thermal-conductivity half-Heusler semiconductors via high-throughput materials modeling, Phys. Rev. X 4 (1) (2014) 011019.

[25] J. He, M. Amsler, Y. Xia, S.S. Naghavi, V.I. Hegde, S. Hao, S. Goedecker, V. Ozoliņš, C. Wolverton, Ultralow thermal conductivity in full Heusler semiconductors, Phys. Rev. Lett. 117 (4) (2016) 046602.

[26] S. Bhattacharya, A. Pope, R. Littleton IV, T.M. Tritt, V. Ponnambalam, Y. Xia, S. Poon, Effect of Sb doping on the thermoelectric properties of Ti-based half-Heusler compounds, TiNiSn 1- x sb x, Appl. Phys. Lett. 77 (16) (2000) 2476–2478.

[27] J. Herbst, M. Meyer, Structural, electronic, and hydriding properties of Li2MgSi, J. Alloys Compd. 492 (1–2) (2010) 65–68.

[28] D. Stoiber, M. Bobnar, P. Höhn, R. Niewa, Lithium alkaline earth tetrelides of the type Li2AeTt (Ae=Ca, Ba, Tt= Si, Ge, Sn, Pb): Synthesis, crystal structures and physical properties, Z. Naturforschung B 72 (11) (2017) 847–853.

[29] S.E. Gulebaglan, Structural electronic and vibrational properties analysis of Li2CaX (X= Sn, Pb) heusler alloys: a comparative study, Mater. Res. Express 7 (5) (2020) 056523.

[30] Efficiency of ab-initio total energy calculations for metals and semiconductors using a plane-wave basis set, Comput. Mater. Sci. (ISSN: 0927-0256) 6 (1) (1996) 15–50.

[31] G. Kresse, J. Furthmüller, Efficient iterative schemes for ab initio total-energy calculations using a plane-wave basis set, Phys. Rev. B 54 (1996) 11169–11186.

[32] J.P. Perdew, K. Burke, M. Ernzerhof, Generalized gradient approximation made simple, Phys. Rev. Lett. 77 (1996) 3865–3868.

[33] J.-L. Calais, Density-functional theory of atoms and molecules. R.G. Parr and W. Yang, Oxford University Press, New York, Oxford, 1989. IX + 333 pp. Price £45.00, Int. J. Quantum Chem. 47 (1) 101–101.

[34] H.J. Monkhorst, J.D. Pack, Special points for Brillouin-zone integrations, Phys. Rev. B 13 (1976) 5188–5192.

[35] P.E. Blöchl, O. Jepsen, O.K. Andersen, Improved tetrahedron method for Brillouin-zone integrations, Phys. Rev. B 49 (1994) 16223–16233.

[36] A. Togo, F. Oba, I. Tanaka, First-principles calculations of the ferroelastic transition between rutile-type and CaCl 2-type SiO 2 at high pressures, Phys. Rev. B 78 (13) (2008) 134106.

[37] N. Marzari, D. Vanderbilt, Maximally localized generalized wannier functions for composite energy bands, Phys. Rev. B 56 (1997) 12847–12865.

[38] An updated version of wannier90: A tool for obtaining maximally-localised wannier functions, Comput. Phys. Comm. (ISSN: 0010-4655) 185 (8) (2014) 2309–2310.

[39] Q. Wu, S. Zhang, H.-F. Song, M. Troyer, A.A. Soluyanov, WannierTools: An open-source software package for novel topological materials, Comput. Phys. Comm. 224 (2018) 405–416.

[40] M.P.L. Sancho, J.M.L. Sancho, J.M.L. Sancho, J. Rubio, Highly convergent schemes for the calculation of bulk and surface green functions, J. Phys. F Metal Phys. 15 (4) (1985) 851–858.

[41] A. Togo, L. Chaput, I. Tanaka, Distributions of phonon lifetimes in Brillouin zones, Phys. Rev. B 91 (9) (2015) 094306.

[42] J. Heyd, G.E. Scuseria, M. Ernzerhof, Hybrid functionals based on a screened Coulomb potential, J. Chem. Phys. 118 (18) (2003) 8207–8215.

[43] BoltzTraP. A code for calculating band-structure dependent quantities, Comput. Phys. Comm. (ISSN: 0010-4655) 175 (1) (2006) 67–71.

[44] F. Mouhat, F.-X. Coudert, Necessary and sufficient elastic stability conditions in various crystal systems, Phys. Rev. B 90 (22) (2014) 224104.

[45] S. Pugh, XCII. Relations between the elastic moduli and the plastic properties of polycrystalline pure metals, Lond. Edinburgh Dublin Philos. Mag. J. Sci. 45 (367) (1954) 823–843.

[46] O.L. Anderson, A simplified method for calculating the debye temperature from elastic constants, J. Phys. Chem. Solids 24 (7) (1963) 909–917.

[47] C. Fang, Y. Chen, H.-Y. Kee, L. Fu, Topological nodal line semimetals with and without spin-orbital coupling, Phys. Rev. B 92 (8) (2015) 081201.

[48] S.S. Shastri, S.K. Pandey, Two functionals approach in DFT for the prediction of thermoelectric properties of Fe2ScX (X=P, As, Sb) full-Heusler compounds, J. Phys.: Condens. Matter 31 (43) (2019) 435701.

[49] B.G. Yalcin, Ground state properties and thermoelectric behavior of Ru2VZ (Z=Si, ge, sn) half-metallic ferromagnetic full-Heusler compounds, J. Magn. Magn. Mater. 408 (2016) 137–146.

[50] G. Remil, A. Zitouni, B. Bouadjemi, M. Houari, A. Abbad, W. Benstaali, S. Cherid, M. Matougui, T. Lantri, S. Bentata, A potential full Heusler thermoelectric material CO2ZrZ (Z=Al, Si, Ga and Sn) in low temperature: An Ab-initio investigation, Solid State Commun. 336 (2021) 114422.

[51] S. Mondal, C. Mazumdar, R. Ranganathan, E. Alleno, P. Sreeparvathy, V. Kanchana, G. Vaitheeswaran, Ferromagnetically correlated clusters in semimetallic Ru 2 NbAl Heusler alloy and its thermoelectric properties, Phys. Rev. B 98 (20) (2018) 205130.

[52] M.K. Yadav, B. Sanyal, First principles study of thermoelectric properties of Li-based half-Heusler alloys, J. Alloys Compounds 622 (2015) 388–393.

[53] M. Zhang, J. Wei, G. Wang, Thermoelectric and topological properties of half-Heusler compounds ZrIrX (As, Sb, Bi), Phys. Lett. A 382 (9) (2018) 673–678.

[54] S.A. Khandy, J.-D. Chai, Origin of pseudo gap and thermoelectric signatures of semimetallic Ru2TaGa: Structural stability from phonon dynamics, mechanical, and thermodynamic predictions, J. Phys. Chem. Solids 154 (2021) 110098.